

RESULTS FROM EDGES HIGH-BAND:
 I. CONSTRAINTS ON PHENOMENOLOGICAL MODELS FOR THE GLOBAL 21 CM SIGNAL

RAUL A. MONSALVE^{1,2}, ALAN E. E. ROGERS³, JUDD D. BOWMAN², AND THOMAS J. MOZDZEN²

¹Center for Astrophysics and Space Astronomy, University of Colorado, Boulder, CO 80309, USA; Raul.Monsalve@colorado.edu

²School of Earth and Space Exploration, Arizona State University, Tempe, AZ 85287, USA and

³Haystack Observatory, Massachusetts Institute of Technology, Westford, MA 01886, USA

Draft version August 22, 2017

ABSTRACT

We report constraints on the global 21 cm signal due to neutral hydrogen at redshifts $14.8 \geq z \geq 6.5$. We derive our constraints from low foreground observations of the average sky brightness spectrum conducted with the EDGES High-Band instrument between September 7 and October 26, 2015. Observations were calibrated by accounting for the effects of antenna beam chromaticity, antenna and ground losses, signal reflections, and receiver parameters. We evaluate the consistency between the spectrum and phenomenological models for the global 21 cm signal. For tanh-based representations of the ionization history during the epoch of reionization, we rule out, at $\geq 2\sigma$ significance, models with duration of up to $\Delta z = 1$ at $z \approx 8.5$ and higher than $\Delta z = 0.4$ across most of the observed redshift range under the usual assumption that the 21 cm spin temperature is much larger than the temperature of the cosmic microwave background (CMB) during reionization. We also investigate a ‘cold’ IGM scenario that assumes perfect Ly α coupling of the 21 cm spin temperature to the temperature of the intergalactic medium (IGM), but that the IGM is not heated by early stars or stellar remnants. Under this assumption, we reject tanh-based reionization models of duration $\Delta z \lesssim 2$ over most of the observed redshift range. Finally, we explore and reject a broad range of Gaussian models for the 21 cm absorption feature expected in the First Light era. As an example, we reject 100 mK Gaussians with duration (full width at half maximum) $\Delta z \leq 4$ over the range $14.2 \geq z \geq 6.5$ at $\geq 2\sigma$ significance.

Keywords: early universe — cosmology: observations — methods: data analysis

1. INTRODUCTION

Illuminating the early stellar history is important for understanding the origin and evolution of structure in the Universe. The first luminous sources emitted UV and X-ray radiation that ionized and heated the diffuse neutral hydrogen gas in the intergalactic medium (IGM). Stars are believed to be responsible for the bulk of the UV photons, while the primary sources of X-rays are still largely uncertain, but usually assumed to be stellar remnants (Barkana & Loeb 2001; Furlanetto et al. 2006b; Pritchard & Loeb 2012; Mesinger et al. 2013; Madau & Haardt. 2015; Fialkov et al. 2016b; Greig & Mesinger 2017a).

Low frequency radio observations of the redshifted 21 cm line of neutral hydrogen gas represent a unique avenue for observationally constraining the radiative properties of the first luminous objects and the reionization history of the Universe (Madau et al. 1997; Furlanetto et al. 2006b). In particular, the sky average or ‘global’ 21 cm signal is expected to provide essential information through the mean properties of the IGM at $z \gtrsim 6$ (Shaver et al. 1999; Gnedin & Shaver 2004; Mirocha et al. 2013, 2015; Fialkov & Loeb 2016a). The brightness temperature of the global 21 cm signal is modeled as (Zaldarriaga et al. 2004)

$$T_{21}(z) \approx 28 x_{\text{HI}}(z) \left[\frac{T_s(z) - T_{\text{cmb}}(z)}{T_s(z)} \right] \sqrt{\frac{1+z}{10}} \text{ [mK]}, \quad (1)$$

where T_{cmb} is the temperature of the cosmic microwave background (CMB), x_{HI} is the average fraction of neutral hydrogen in the IGM, and T_s is the spin temperature of the neutral hydrogen, which quantifies the relative abundance of hydrogen atoms in the high and low energy ground state. Information about the radiative properties of the first stars, galaxies, and

black holes is encapsulated in the neutral fraction and spin temperature of the gas and, therefore, can be probed through measurements of the global 21 cm brightness temperature. Since redshift maps to frequency for the 21 cm line according to $\nu = 1420 \text{ MHz}/(1+z)$, the brightness temperature for redshifts $\gtrsim 6$ is measured at frequencies $\lesssim 200 \text{ MHz}$ in the VHF radio band.

Most models for the global 21 cm signal contain two dominant features once star formation commences (Shaver et al. 1999; Gnedin & Shaver 2004; Furlanetto et al. 2006a; Mesinger et al. 2013; Sitwell et al. 2014; Tanaka et al. 2016; Kaurov & Gnedin 2016; Fialkov et al. 2016b; Mirocha et al. 2017; Cohen et al. 2017). First, the models predict an approximately Gaussian-shaped absorption trough during the First Light era. This trough is initiated at $z \gtrsim 15$ with the onset of coupling of the spin temperature to the cold kinetic temperature of the IGM, T_{IGM} , by UV photons from the first sources (Wouthuysen 1952; Field 1958). The trough usually concludes with the subsequent heating of the IGM above the CMB temperature by X-rays from the early stellar remnants in the models. The second global 21 cm spectral feature is expected during the epoch of reionization (EoR, $z \lesssim 10$), when neutral hydrogen—and therefore the 21 cm signal—is gradually extinguished by UV radiation from the increasing number of sources. The evolution of the neutral fraction in the models during reionization often exhibits a functional form similar to a hyperbolic tangent.

This general scenario for the evolution of the IGM and the global 21 cm signal is consistent among many theoretical models. However, because the specific properties of early stars and stellar evolution remain unknown, the timing, duration, and amplitude of the 21 cm features all vary between models. In most cases, for models based on stellar and galac-

tic properties extrapolated from existing observations, reionization occurs after the IGM has been heated well above the CMB temperature and the 21 cm signal is in emission. In some cases, however, reionization takes place without substantial heating and while the 21 cm signal is still in absorption. Typically, the absorption trough and reionization transition in the global 21 cm signal have expected amplitudes of tens to hundreds of mK.

The Experiment to Detect the Global EoR Signature (EDGES) aims to detect the global 21 cm signal through single antenna radio observations. It has placed the most significant lower limit on the duration of reionization to date, of $\Delta z > 0.06$ at 95% confidence (Bowman & Rogers 2010a). Ongoing developments in instrumentation and calibration have improved the performance of the system, as well as enabled EDGES to contribute to the characterization of astronomical foregrounds and Earth’s ionosphere (Rogers & Bowman 2008, 2012; Rogers et al. 2015; Mozdzen et al. 2016; Monsalve et al. 2016; Mozdzen et al. 2017; Monsalve et al. 2017). EDGES currently operates two total power spectral radiometers, identified as Low-Band and High-Band, which cover the ranges 50–100 MHz ($27.4 \gtrsim z \gtrsim 13.2$) and 90–190 MHz ($14.8 \gtrsim z \gtrsim 6.5$), and nominally target the features from First Light and the reionization, respectively. They observe from the Murchison Radio-astronomy Observatory (MRO) in Western Australia, taking advantage of its radio-quiet environment (Bowman & Rogers 2010b; Offringa et al. 2015).

Several other experiments are also pursuing measurement of the global 21 cm signal. Using 4.4 hours of data, SCI-HI reported limits in the form of 1 K rms residuals in the range 60–88 MHz after subtracting the foregrounds using a three term log-log polynomial (Voytek et al. 2014). LEDA, using 19 minutes of effective measurements, placed limits on the absorption trough between 50 and 100 MHz in the form of 95% constraints on the amplitude (> -890 mK) and 1σ width (> 6.5 MHz) of a Gaussian model for the trough (Bernardi et al. 2016). The SARAS 2 experiment (Singh et al. 2017) has recently ruled out at 1σ several models of the global 21 cm signal during the reionization era that were generated from the semi-numerical simulations of Cohen et al. (2017). Finally, the DARE space mission is planning to measure the global 21 cm signal from orbit above the far side of the Moon (Burns et al. 2017).

In this paper we present constraints on the global 21 cm signal from measurements conducted with EDGES High-Band between September 7 and October 26, 2015. The data consist of 40 nighttime observations over the low foreground region 0.26–6.26 hr local sidereal time (LST). They are processed through a pipeline that performs instrumental calibration and excision of data contaminated with radio-frequency interference (RFI). The data are then averaged in time and binned in frequency to obtain the final sky temperature spectrum.

We use the average spectrum to probe phenomenological models for the global 21 cm signal. Specifically, we probe the allowed duration of reionization under two end-member cases of the IGM thermal evolution. Our two thermal cases are: (1) the standard ‘hot’ IGM scenario where early stars and stellar remnants have heated the IGM before reionization such that the gas kinetic temperature is $T_{\text{IGM}} \gg T_{\text{cmb}}$, and (2) a ‘cold’ IGM with no heating from stars or stellar remnants before or during reionization, such that the gas kinetic temperature history is given by the adiabatic expansion of the Universe. In both cases we assume $T_s = T_{\text{IGM}}$ (Ciardi & Madau 2003; Pritchard & Furlanetto 2007) and we represent the ionization history

(x_{HI}) with functional forms drawn from hyperbolic tangents. We also conduct a general test of absorption signals expected from First Light using models of absorption trough features based on a broad set of symmetrical and skewed Gaussians. For all of our phenomenological cases, our full measurement model includes polynomial terms to account for foregrounds and calibration systematics, in addition to the 21 cm contribution. We estimate our sensitivity to calibration uncertainties by propagating uncertainty estimates through the analysis pipeline.

This paper is organized as follows. Section 2 describes the EDGES High-Band instrument and calibration. Section 3 presents the data analyzed and the strategy for constraining phenomenological parameters. Section 4 presents the main results of this paper, in the form of constraints on the tanh and Gaussian models, and discusses the impact of conservative calibration uncertainties. Section 5 concludes this work with a summary of the findings.

2. INSTRUMENT

Here we describe the EDGES High-Band instrument, with a focus on the antenna characteristics and calibration. The EDGES High-Band instrument captures sky radiation using a single polarization dipole-like blade antenna (Mozdzen et al. 2016, 2017). This antenna is composed of two rectangular aluminum panels of dimensions 62.5 cm \times 48.1 cm, mounted horizontally at a height of 52 cm above a metal ground plane. The separation between the panels is 2.2 cm. The panels are supported by a lightweight structure composed of hollow square fiberglass pipes and teflon rods. The metal ground plane rests on the physical ground and consists of a solid aluminum central square of 5.35 m \times 5.35 m and four wiregrid panels of size 5 m \times 2 m attached to the sides of the solid square. The excitation axis of the antenna is orientated -5° from the North-South axis. The antenna beam points at the zenith and has a full width at half maximum (FWHM) at 140 MHz of 72° (108°) parallel (perpendicular) to the excitation axis.

The front-end receiver is located under the ground plane, directly below the antenna. A Roberts balun (Roberts 1957) is used to ground reference the electrically balanced signal induced at the antenna panels and guide it toward the receiver. The balun is implemented as two brass tubes of 0.5" outer diameter connected to the antenna panels, and a copper plated brass rod running up inside one of the tubes. A copper plate connects the rod sticking out of the tube above the antenna panel, with the opposite panel. At the base of the balun the tubes are attached to the ground plane. A small rectangular metal enclosure is also attached to the ground plane to shield against vertical currents in the tubes. The tube containing the rod extends below the ground plane, where it transitions into a teflon dielectric SMA connector that takes the signal to the receiver input.

The front-end receiver is designed around a low-noise amplifier (LNA), plus additional stages of gain, filtering, and conditioning. The input of the LNA switches continuously between: (1) the antenna, (2) an ambient load noise reference, and (3) the ambient load plus an active noise source connected in series to form a second, higher noise reference. The measurements of these two references are used to conduct a relative calibration at the LNA input, which removes the time dependent instrument passband. The duration of the three-position switching cycle is 39 seconds. A back-end amplification unit, located ≈ 100 m away from the antenna/receiver,

provides additional stages of gain, filtering, and conditioning. The output from the back-end is digitized and Fourier transformed at a resolution of 6.1 kHz. We store the power spectral densities from the antenna and the two internal noise references for offline calibration.

The reflection coefficient of the antenna, including the effect of the balun, is a critical parameter in the EDGES calibration approach (Rogers & Bowman 2012; Monsalve et al. 2017). This parameter is measured in the field using a vector network analyzer (VNA), located next to the back-end unit, in coordination with electronics at the front-end receiver. The measurement is conducted remotely, without disconnecting the antenna from the receiver.

2.1. Calibration

To convert the antenna power spectral density measured in the field to a calibrated sky temperature spectrum, we use calibration measurements and models to remove the effects of the following parameters: (1) gain, offset, reflection coefficient, and noise parameters of the receiver, (2) antenna reflection coefficient, (3) antenna and ground losses, and (4) antenna beam chromaticity.

2.1.1. Receiver

We set the input of the receiver as the reference plane for absolute antenna temperature measurements. We calibrate the sky measurements at this plane using six receiver parameters obtained in the laboratory before deployment (Rogers & Bowman 2012; Monsalve et al. 2016, 2017). During laboratory calibration and operation in the field, the receiver is maintained at a nominal temperature of 25°C using active control. During the nighttime sky measurements used for this paper, the receiver temperature drifted within $\pm 1^\circ\text{C}$. To remove the effect of these drifts, we conducted an additional laboratory calibration with the receiver temperature set to 35°C. We use the two laboratory results to calibrate the sky measurements using receiver parameters interpolated (or extrapolated) linearly to the measured temperature of the receiver.

2.1.2. Antenna Reflection Coefficient

We measured in the field the reflection coefficient of the antenna, including the effect of the balun, during a three-day session starting on September 19, 2015, at a rate of one measurement per minute. The observed nighttime and night-to-night reflection stability is better than ± 0.01 dB and $\pm 0.1^\circ$. This stability is comparable to the intrinsic uncertainty in the VNA reflection measurement (Monsalve et al. 2016, 2017). Therefore, we average all 29 hours of nighttime measurements from the session to derive our fiducial antenna reflection coefficient.

We fit the reflection magnitude and phase using 16 term polynomials in frequency in order to remove noise and interpolate the reflection to the same frequency channels as the sky spectra. These models capture all significant structure in the data and produce rms fit residuals of 0.004 dB and 0.03° . Figure 1 (a) shows the magnitude and phase of the antenna reflection coefficient.

2.1.3. Antenna and Ground Losses

After calibrating the antenna temperature at the receiver input, we need to remove from the spectrum the effect of losses in the antenna panels (L_a), the balun (L_b) and connector to the receiver (L_c), as well as ground losses due to non zero

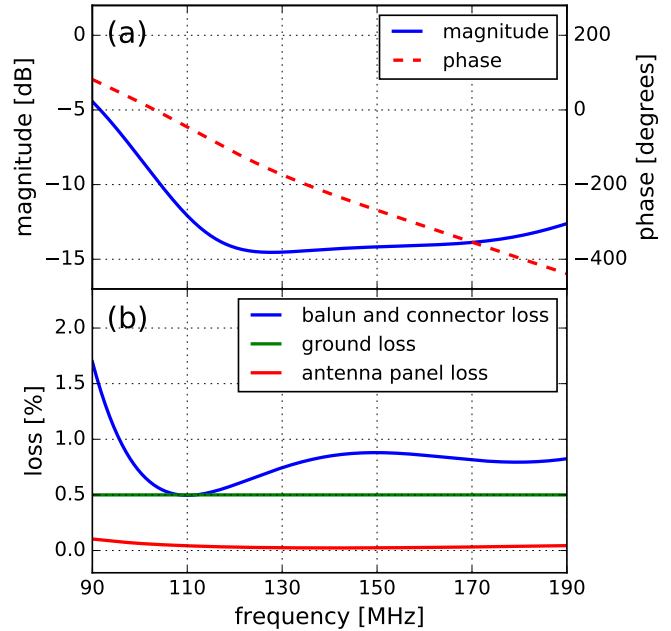


Figure 1. (a) Polynomial fits to the measured antenna reflection coefficient magnitude and phase as discussed in Section 2.1.2. (b) Fiducial antenna and ground losses described in Section 2.1.3 and used to correct the measured spectra.

beam directivity below the horizon (L_g). The measured antenna temperature affected by losses, T_{ant}^L , is given by

$$T_{\text{ant}}^L = LT_{\text{ant}} + (1-L)T_{\text{amb}}, \quad (2)$$

where T_{ant} is the antenna temperature before losses, T_{amb} is the ambient temperature, and $L = L_a L_b L_c L_g$ represents the combined loss, which takes values between 0 and 1 where 1 represents no loss.

The antenna panels are affected by resistive losses. We estimate this small effect from electromagnetic simulations with the FEKO software package¹. Balun and connector loss occurs along the conductors, as well as through their air and teflon dielectric, respectively. We estimate these losses from analytical models of these cylindrical transmission lines, and check these models using reflection measurements of an open and shorted balun.

We initially estimate the ground loss from our beam model computed with FEKO (Section 2.1.4). Due to the simulation complexities and uncertainties in this small effect, we conduct an additional simulation with the CST package². The FEKO simulation employs Greens functions to model our finite metal ground plane over an infinite soil (infinite in $\pm\hat{x}$, $\pm\hat{y}$, and toward $-\hat{z}$). The soil is characterized in terms of its conductivity and relative permittivity, with nominal values of 0.02 Sm^{-1} and 3.5, respectively, as estimated by Sutinjo et al. (2015) for the dry conditions at the MRO. The CST simulation incorporates the ground plane but not the soil, representing a boundary scenario for the estimation of the beam fraction below the horizon. The two simulations produce an average loss of 0.5% across the band, but with a different spectral profile. Therefore, we take as our nominal ground loss a spectrally flat profile with a value of 0.5%. Figure 1 (b) shows our fiducial

¹ www.feko.info

² www.cst.com

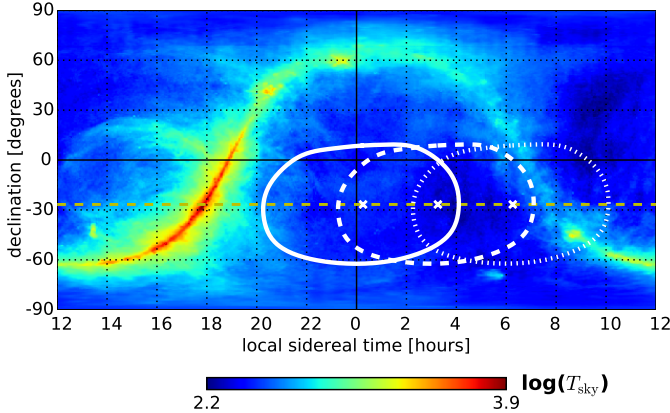


Figure 2. Three reference projections of the 140 MHz EDGES antenna beam FWHM onto the low foreground sky seen from the EDGES latitude of -26.72° (dashed yellow line). In this paper, we use observations over the continuous LST range 0.26–6.26 hr. The three beam snapshots correspond to pointings at LST = 0.26 hr (solid white), 3.26 hr (dashed white), and 6.26 hr (dotted white).

antenna and ground losses.

2.1.4. Beam Chromaticity

Beam chromaticity describes spectral variations of the antenna beam that introduce structure to the sky temperature spectrum (Vedantham et al. 2014; Bernardi et al. 2015; Mozdzen et al. 2016). The calibrated sky temperature spectrum, T_{sky} , is obtained by removing the effect of beam chromaticity from the lossless antenna temperature, T_{ant} . We model this effect through a multiplicative chromaticity factor C that relates the two temperatures as

$$T_{\text{ant}}(\text{LST}, \nu) = C(\text{LST}, \nu) \cdot T_{\text{sky}}(\text{LST}, \nu). \quad (3)$$

The chromaticity factor is computed as

$$C(\text{LST}, \nu) = \frac{\int \hat{B}(\nu, \Omega) \hat{T}_{\text{sky}}(\text{LST}, \nu, \Omega) d\Omega}{\int \hat{B}(\nu_n, \Omega) \hat{T}_{\text{sky}}(\text{LST}, \nu_n, \Omega) d\Omega}, \quad (4)$$

where Ω represents spatial coordinates above the horizon, \hat{B} represents our beam model, and \hat{T}_{sky} is a model for the diffuse sky visible from the MRO (different from our calibrated sky temperature spectrum, T_{sky}).

The numerator in Equation (4) corresponds to the convolution of the frequency-dependent beam and sky, while the denominator represents a convolution where the beam is evaluated at a specific frequency ν_n . Thus, by design, the denominator normalizes C to one at $\nu = \nu_n$. At other frequencies, C departs from one due to a beam pattern that changes with frequency. The normalization frequency is chosen as the middle of the band, i.e., 140 MHz. The chromaticity factor only removes the corruption introduced by a frequency-dependent beam. It does not intend to force a match between the calibrated sky spectrum, T_{sky} , and the spectrum predicted from the sky model.

We obtain our beam model from electromagnetic simulations with FEKO, which are also used to estimate some of the loss terms (Section 2.1.3). Our sky model consists of the 408 MHz Haslam map (Haslam et al. 1982) scaled to the range 90–190 MHz using a spatially dependent spectral index computed using the Haslam map and the Guzmán map at 45 MHz (Guzmán et al. 2011). In Mozdzen et al. (2017) we found that this simple model produces the closest match to

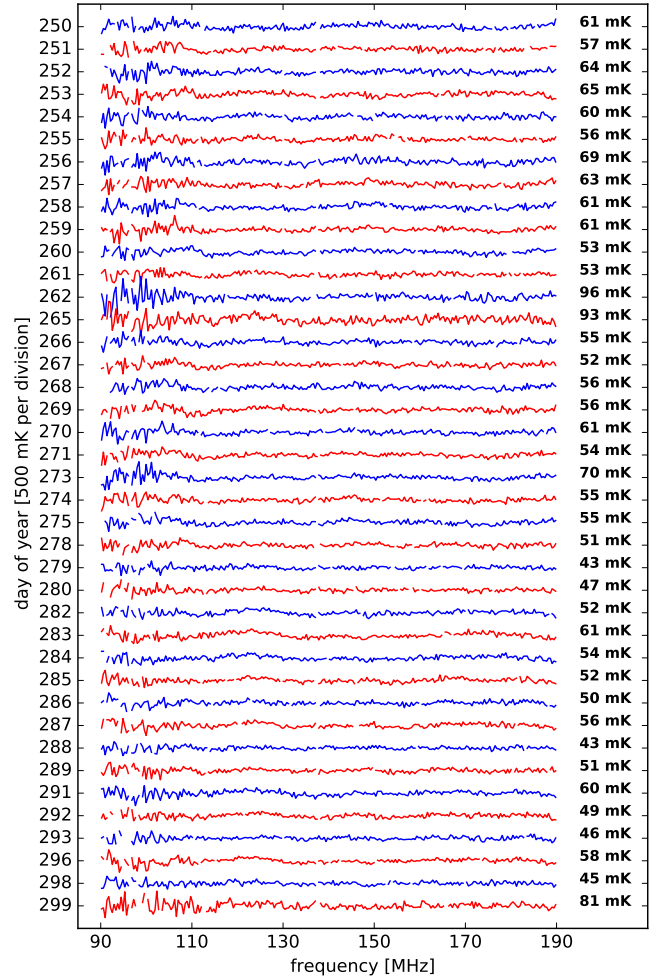


Figure 3. Residuals of integrated spectra after five-term polynomial fits. As described in Section 3.1, in our analysis we use nighttime observations conducted between September 7 and October 26, 2015, over the LST range 0.26–6.26 hr. Each row represents the residuals of the integrated spectrum for a different night. The rms of each residual spectrum is listed to the right and calculated with a frequency binning of 390.6 kHz and weighted by the number of samples per bin. The residual rms for each night varies between 43 and 96 mK.

our observed diffuse foreground spectra. The sky model does not include the global 21 cm signal, which has an insignificant effect on the chromaticity correction.

Figure 2 shows the FWHM of the beam model projected onto the sky model at 140 MHz.

3. DATA ANALYSIS

In this section we describe the data and our strategy for probing the 21 cm models.

3.1. Calibrated Spectrum

The data used in this analysis correspond to 40 nighttime observations, with the Sun at least 10° below the horizon, covering the LST range 0.26–6.26 hr. On the first day in our set, September 7, the coverage is only 0.26–4.5 hr, which increases gradually and reaches 0.26–6.26 hr on October 14. Since then, it remains constant until our last day, October 26.

We start the analysis by evaluating the structure and stability of the daily average spectra. For each daily data set, we (1) calibrate all 39-second spectra, (2) average the spectra over LST 0.26–6.26 hr, and (3) bin the average spectrum

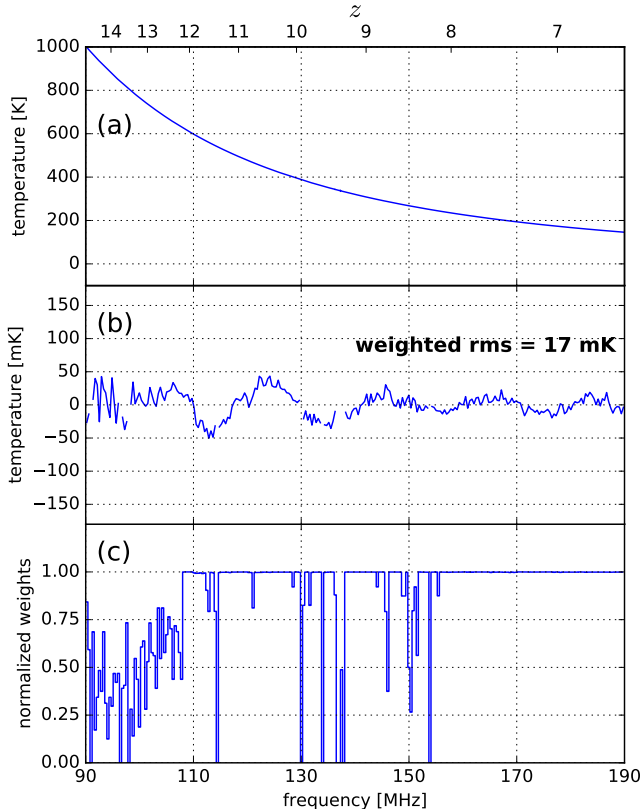


Figure 4. (a) Total spectrum, integrated over LST 0.26–6.26 hr. (b) Residuals of the integrated spectrum to a five-term polynomial fit. The weighted rms is 17 mK. The rms of thermal noise alone above 108 MHz is 6 mK. Much of the observed ripple structure is non-thermal. (c) Normalized weights for each 390.6 kHz spectral channel bin in the full integrated spectrum. The weights are the fraction of raw samples in each bin compared to the maximum number of raw samples per bin, of approximately 1.2×10^6 . Variations in weight from channel to channel are due primarily to RFI excision, which is most pronounced in the FM radio band (below 108 MHz).

into 390.6 kHz channels (64 raw channels of 6.1 kHz width). In parallel, we excise raw channels contaminated with RFI. RFI is identified by averaging data on different time scales, between the shortest (39 s) and the daily (> 4 hr) integrations, and performed both, before and after spectral binning.

Then, to evaluate the quality and stability of the calibration we remove the contribution of diffuse foregrounds from each daily spectrum. Although to first order the foregrounds are well modeled by a power law (Mozdzen et al. 2017), to reach the mK level targeted for the 21 cm measurement the model requires additional terms (Kogut 2012; Voytek et al. 2014; Bernardi et al. 2015, 2016; Sathyanarayana Rao et al. 2017). We find that five polynomial terms are necessary to reduce the fit residuals to our daily noise level over the 90–190 MHz range. Our polynomial foreground model is:

$$\hat{T}_{\text{fg}}(\nu) = \sum_{i=0}^4 a_i \nu^{-2.5+i}. \quad (5)$$

Figure 3 shows the single-day residuals to the five-term polynomial fit, as well as their weighted rms over frequency. In most cases the residuals are dominated by noise. Their rms fluctuates between 43 mK and 96 mK, with a median of 56 mK. The day-to-day variations are attributed to (1) intrinsic noise variance, (2) different effective integration time due to

different LST coverages, RFI excision, or bad weather cuts, and (3) any unaccounted for variations in instrument response not corrected in the calibration.

Next, we evaluate the structure and stability of the spectrum for longer integrations. We perform many trials of 20-day averages (about 50% of total data), selecting days randomly for each trial. We see that the residual structure to a five-term polynomial fit is consistent between the trials, with rms differences < 4 mK.

Finally, we compute the total average spectrum. We average in time all the daily measurements at raw frequency resolution, and then bin the spectrum at 390.6 kHz. In parallel we conduct the RFI excision, which is extended to time scales between several hours and the full set. The largest number of raw samples per frequency bin in the final spectrum is approximately 1.2×10^6 (with each sample representing 39 s, 6.1 kHz).

Figure 4 (a) shows the total average spectrum, which has a brightness temperature ≈ 998 K at 90 MHz and ≈ 146 K at 190 MHz. Figure 4 (b) shows the residuals of the average spectrum to a five-term polynomial fit, and Figure 4 (c) shows the normalized number of samples per bin. The residuals have a weighted rms of 17 mK over 90–190 MHz. Above 108 MHz, the rms of the thermal noise alone is 6 mK, computed from the channel-to-channel differences. Below 108 MHz, the thermal noise is higher due to increased RFI excision in the FM radio band. The non-thermal systematic structure can be described as ripples with a period of ≈ 20 MHz and an amplitude that decreases with frequency. This pattern resembles the effect of small errors in the reflection coefficient of the receiver and antenna, as explored in Monsalve et al. (2017). Our analysis described below accounts for systematic uncertainties and is designed to reduce sensitivity to any residual calibration errors in the spectrum by performing parameter estimation trials on the spectrum within windows of different widths and centers, as well as by using different numbers of foreground terms. We will further explore the effects of possible calibration errors on our results in Section 4.4.

3.2. Model Rejection Approach

Following Bowman & Rogers (2010a), we will report 21 cm models that can be rejected at a given significance. We start by modeling the sky brightness temperature spectrum as:

$$T_{\text{sky}} = \hat{T}_{21} + \hat{T}_{\text{fg}} + \text{noise}, \quad (6)$$

where T_{sky} is the observed spectrum data, \hat{T}_{21} is one of the 21 cm models, described in Section 4, and \hat{T}_{fg} is the foreground model of Equation (5).

The fit parameters in this model are the amplitude of the 21 cm model, a_{21} , and the polynomial coefficients of the foreground model, a_i . We estimate the vector of linear parameters, $\lambda = [a_{21}, a_i]$, and their covariance matrix, Σ , using weighted least squares:

$$\hat{\lambda} = (A^T W A)^{-1} A^T W T_{\text{sky}}, \quad (7)$$

$$\hat{\Sigma} = s^2 (A^T W A)^{-1}. \quad (8)$$

Here, A is the design matrix, with columns that correspond to the normalized 21 cm model and the polynomial terms of the foreground model, and W is a diagonal matrix of relative

weights, with diagonal elements equal to the number of samples per frequency bin. The s^2 factor is the weighted sum of squared residuals normalized by the degrees of freedom,

$$s^2 = \frac{r^T W r}{N_\nu - N_\lambda - 1}, \quad (9)$$

where N_ν is the number of frequency bins, N_λ is the number of parameters, and r is the difference between the data and the best-fit model.

To determine if a 21 cm model can be rejected, we evaluate the consistency of the least squares amplitude estimate for the model, \hat{a}_{21} , with zero and with the expected model amplitude, T_{ref} . We reject the model if the amplitude estimate satisfies $|\hat{a}_{21}| < T_{\text{ref}}/2$. We further limit the set of rejected models reported here to only those that can be detected when they are artificially injected into the data. All rejections presented in this paper satisfy these conditions. The significance of the rejection is given by:

$$\text{rejection significance} = \frac{T_{\text{ref}} - \hat{a}_{21}}{\hat{\sigma}_{21}}, \quad (10)$$

where $\hat{\sigma}_{21} = \hat{\Sigma}_{11}^{1/2}$ is the least squares amplitude uncertainty estimate from the model fit.

We report rejections with significance equal to or higher than 1σ . Models could fail to be rejected for two reasons. First, the fit amplitude, \hat{a}_{21} , could be far from zero (i.e., $|\hat{a}_{21}| \geq T_{\text{ref}}/2$) because the 21 cm model fits structure in the integrated spectrum from either an actual 21 cm signal or calibration errors. Second, the fit uncertainty, $\hat{\sigma}_{21}$, could be large due to high residuals from thermal noise or residual structure from using an imperfect signal model, or, due to high covariance between the 21 cm and foreground models, which is likely, for example, with slow reionization scenarios. In particular, when we simultaneously fit the parameters $\lambda = [a_{21}, a_i]$, the estimate \hat{a}_{21} does not systematically decrease as we increase the number of polynomial terms. Instead, it takes values consistent with larger uncertainty due to higher covariance.

To maximize the sensitivity to the 21 cm model through minimizing the residuals and covariances, we adjust the frequency range and the number of foreground parameters in the fit. We compute multiple least squares estimates of \hat{a}_{21} and $\hat{\sigma}_{21}$ for each trial 21 cm model by exploring multiple choices of the frequency range and foreground parameters. We try (1) spectral windows of different widths between 20 and 100 MHz, (2) sweeping the window across the spectrum in steps equal to the frequency channel width (390.6 kHz), and (3) varying the number of foreground terms between two and five. In the results below, we report the rejection significance obtained for the fit conditions that produce the lowest 21 cm amplitude uncertainty.

4. RESULTS

Here we describe our findings for the three sets of 21 cm models tested. They correspond to phenomenological models for the reionization transition assuming the two end-member cases for the heating states of the IGM, as well as a generic model for the absorption trough from the First Light era. Figure 5 shows a sample of these models.

4.1. Hot IGM Reionization

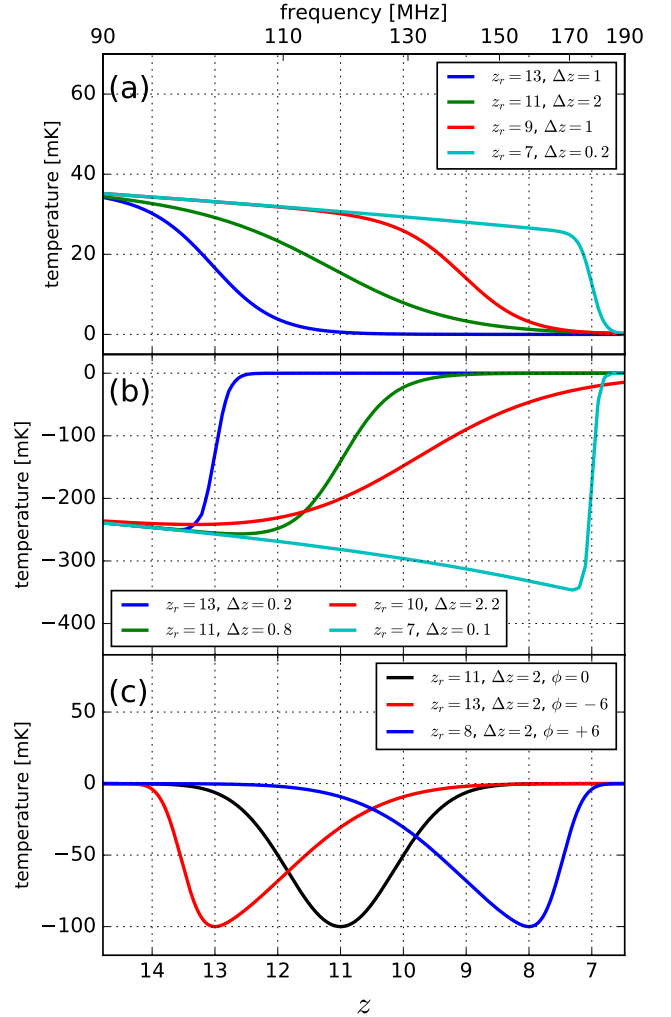


Figure 5. Sample of phenomenological models representing the brightness temperature of the global 21 cm signal. (a) The top panel shows four models illustrating ‘hot’ IGM reionization scenarios that assume efficient heating so that $T_s \gg T_{\text{cmb}}$ and use a tanh-based form for the evolution of neutral fraction, x_{HI} . (b) The middle panel shows models illustrating ‘cold’ IGM reionization scenarios that assume no heating and also use a tanh-based form for x_{HI} . (c) The bottom panel shows symmetrical and skewed Gaussian models for the absorption trough feature expected during the First Light era. In the Gaussian models, Δz represents the FWHM of the Gaussian.

As discussed earlier, many models for the 21 cm signal during reionization find that the IGM has been heated by X-rays to substantially above the CMB temperature (e.g., Pritchard & Loeb 2012; Mesinger et al. 2013). It is also found that the spin temperature is well coupled to the gas temperature by reionization. Hence, in many cases, it is sufficient to approximate the detailed astrophysical models by assuming $T_s \gg T_{\text{cmb}}$ (Furlanetto et al. 2006a,b). We follow this convention and first model the 21 cm brightness temperature for the reionization transition assuming X-ray heating of the IGM before the beginning of reionization. With this assumption, Equation (1) yields a simplified brightness temperature model:

$$\hat{T}_{21}(z) = a_{21} x_{\text{HI}}(z) \sqrt{\frac{1+z}{10}}. \quad (11)$$

We complete the model by representing the average neutral hydrogen fraction, x_{HI} , with the popular redshift-symmetric tanh expression (e.g., Bowman & Rogers 2010a; Pritchard

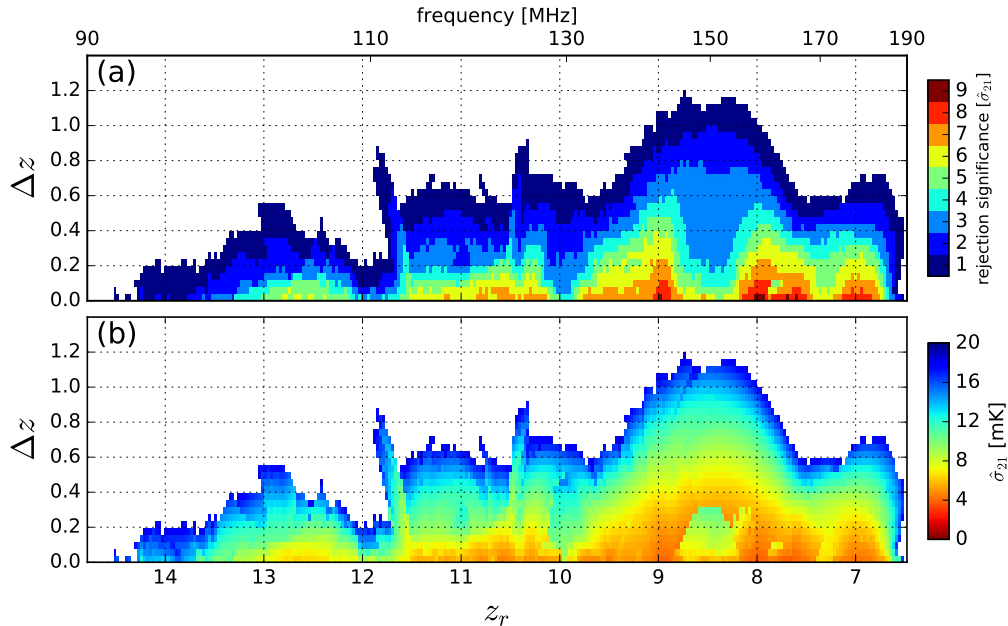


Figure 6. Constraints on reionization from EDGES High-Band assuming a hot IGM and a tanh-based form for the evolution of the neutral fraction, x_{HI} . The reference amplitude of the 21 cm model is $T_{\text{ref}} = 28$ mK. Parameters z_r and Δz indicate the redshift at 50% reionization and the duration of reionization, respectively. Colored regions represent models that are ruled out. (a) The top panel shows the model rejection significance with the color indicating discrete multiples of $\hat{\sigma}_{21}$. (b) The bottom panel shows the corresponding values of $\hat{\sigma}_{21}$. We reject models over the range $14.4 \geq z_r \geq 6.6$, with a peak 2σ rejection of $\Delta z = 1.0$ at $z_r \approx 8.5$.

& Loeb 2010; Morandi & Barkana 2012; Liu et al. 2013; Mirocha et al. 2015; Harker et al. 2016),

$$x_{\text{HI}}(z) = \frac{1}{2} \left[\tanh \left(\frac{z - z_r}{\Delta z} \right) + 1 \right]. \quad (12)$$

The parameters in this x_{HI} model are the reference redshift for 50% reionization, z_r , and the reionization duration, $\Delta z = (dx_{\text{HI}}/dz)^{-1}|_{x_{\text{HI}}=0.5}$. A similar tanh model for x_{HI} has been used by CMB experiments (Lewis 2008; Hinshaw et al. 2013; Planck Collaboration et al. 2016).

As described in Section 3.2, the only 21 cm fit parameter in our analysis is the brightness temperature amplitude, a_{21} . To determine if a model can be rejected, we compare the amplitude estimate, \hat{a}_{21} , with the model reference temperature shown in Equation (1) of $T_{\text{ref}} = 28$ mK (Madau et al. 1997; Furlanetto et al. 2006b). We explore the $(z_r, \Delta z)$ domain to constrain reionization by sweeping the values of these parameters over the ranges $14.8 \geq z_r \geq 6.5$ and $0 \leq \Delta z \leq 2$.

Figure 6 presents the rejection region for the hot IGM reionization models. In the top panel, the colors represent rejections at different discrete significance levels, between 1σ and 9σ . For example, rejections in the range $[1\sigma, 2\sigma]$ are presented as 1σ . The bottom panel shows the corresponding amplitude uncertainties $\hat{\sigma}_{21}$. The uncertainties are lower than 18 mK; specifically, for rejections at $\geq 2\sigma$ they are ≤ 14 mK, and for the peak 9σ rejections they are ≈ 4 mK. In all the rejections, \hat{a}_{21} is consistent with zero to within $\pm 2\hat{\sigma}_{21}$ and the injection test yields amplitude estimates $\hat{a}_{21}^{\text{inj}} > 2\hat{\sigma}_{21}$. As evident in the figure, we reject hot IGM reionization models over the range $14.4 \geq z_r \geq 6.6$. The strongest rejections are obtained in the central part of the spectrum due to the low noise and structure. In particular, our best rejection occurs at a redshift $z_r \approx 8.5$ (150 MHz). Here, we reject models with duration $\Delta z \leq 1.0$ at $\geq 2\sigma$ significance. For $z_r = 8.5$ and $\Delta z = 1$, the rejection is obtained from an amplitude estimate

$\hat{a}_{21} = -9.7 \times 10^{-4} \pm 13$ mK, using a 65 MHz data window and three foreground polynomial terms. For four and five polynomial terms, the uncertainties grow to 49 and 59 mK, respectively, reflecting increased covariance due to overfitting. We also rule out, at $\geq 2\sigma$, models with duration $\Delta z \leq 0.8$ over the range $9 \geq z_r \geq 8$ (142–158 MHz) and $\Delta z \leq 0.4$ over $11.7 \geq z_r \geq 6.7$ (112–184 MHz). These reionization constraints represent a significant improvement with respect to our previous results of Bowman & Rogers (2010a).

In Figure 7 we present our new results in the context of existing constraints and estimates for reionization. A series of observations suggest that reionization has completed by $z \approx 6$ (Bouwens et al. 2015), including the Gunn-Peterson trough (Becker et al. 2001; Fan et al. 2006) and the fraction and distribution of ‘dark pixels’ or gaps in the spectra of high redshift quasars (Gallerani et al. 2006; Mesinger et al. 2010; McGreer et al. 2015), the Ly α damping wing absorption by neutral hydrogen in the spectra of quasars and gamma ray bursts (Chornock et al. 2013; Schroeder et al. 2013; Greig et al. 2017b), the decrease in Ly α emission by galaxies at $z > 6$ (Tilvi et al. 2014; Choudhury et al. 2015), and the clustering of Ly α emitters (Ouchi et al. 2010). In the figure, we represent this combined constraint as an upper limit of the form $\Delta z < 2(z_r - 6)$. The South Pole Telescope (SPT), from measurements of the kinetic Sunyaev-Zel’dovich (kSZ) effect imprinted on the $\ell \approx 3000$ angular scales of the CMB power spectrum, estimated a reionization duration of $\Delta z = 1.3$ and the upper limit $\Delta z < 3$ at 68% confidence (George et al. 2015). SPT defined the duration as the difference between the redshifts for ionized hydrogen fractions 0.2 and 0.99, and assumed the CMB optical depth (τ_z) reported by WMAP (Hinshaw et al. 2013). *Planck* recently estimated a reionization redshift $z_r = 8.5^{+1.0}_{-1.1}$ assuming a redshift-symmetric transition (Planck Collaboration et al. 2016). This is the result shown in the figure for reference. Other estimates from *Planck* range

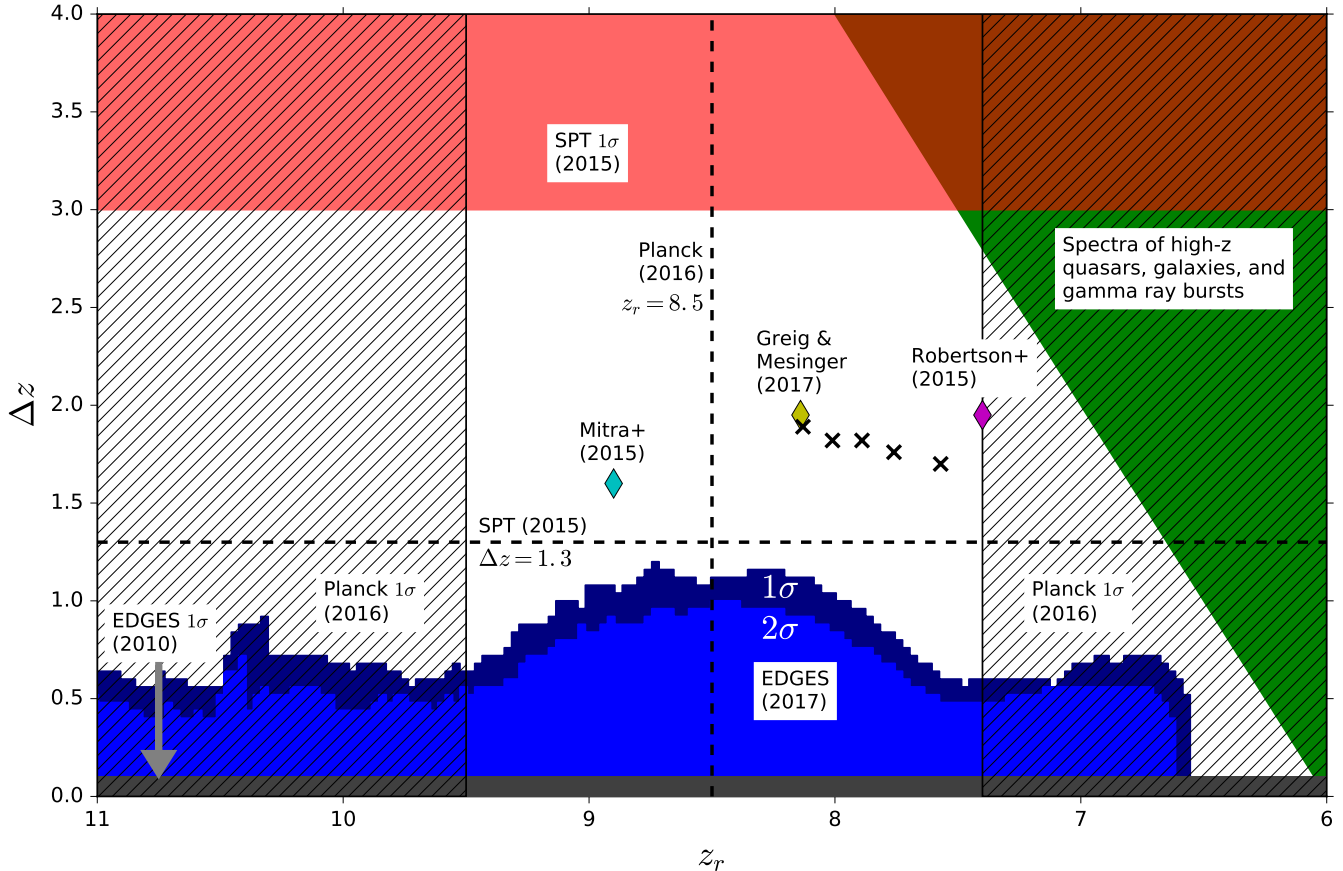


Figure 7. Summary of reionization constraints from existing astrophysical observations. Under the standard assumption of a hot IGM, EDGES rules out reionization models across the range $14.4 \geq z_r \geq 6.6$ (blue region). The peak 2σ rejection corresponds to a duration $\Delta z = 1.0$ at $z_r \approx 8.5$. SPT reported an estimate (horizontal dashed line) and an upper limit (red region) for Δz from measurements of the kSZ power in the CMB power spectrum (George et al. 2015). They defined Δz as the range over which the ionized fraction (i.e., $1 - x_{\text{HI}}$) increases from 0.2 to 0.99, and assumed the CMB optical depth reported by WMAP. The Planck estimate (vertical dashed line) and limits (hatched regions) for z_r shown here assume a redshift-symmetric tanh form for x_{HI} and no prior for the end of reionization redshift (Planck Collaboration et al. 2016). We also show a conservative generic upper limit (green region) of the form $\Delta z < 2(z_r - 6)$ to represent constraints from the spectra of high- z quasars, galaxies, and gamma ray bursts (Bouwens et al. 2015). Finally, we show specific reionization estimates from Robertson et al. (2015) (magenta diamond), Mitra et al. (2015) (cyan diamond), and Greig & Mesinger (2017a) (yellow diamond for their ‘gold sample’ and black crosses for other cases they considered). EDGES provides a unique constraint, ruling out fast reionization scenarios. Modest additional improvements in EDGES performance will make it possible to directly probe the current best estimates for reionization.

from $z_r = 8.8$, derived after applying the prior $z > 6$ for the end of the EoR, to $z_r = 7.2$, combining their temperature and polarization measurements with high- ℓ data from SPT (George et al. 2015) and ACT (Das et al. 2014). We also incorporate in the figure reionization estimates by Robertson et al. (2015), Mitra et al. (2015), and Greig & Mesinger (2017a), which themselves have been derived from different combinations of constraints. In this context, EDGES uniquely contributes to reducing the allowed phenomenological parameter space for a hot IGM reionization by ruling out tanh-based models with duration $\Delta z < 1.2$ at significance levels between 1σ and 9σ .

4.2. Cold IGM Reionization

Next, we probe models produced under the other extreme assumption of no IGM heating by X-rays before or during reionization. This condition results in a large global 21 cm signal observed only in absorption. In particular, the amplitude of 21 cm absorption signal follows the adiabatic cooling of the IGM until, at the low-redshift end, the trough ends purely due to the extinction of neutral hydrogen during reionization.

The cold IGM models are generated analytically by assuming (1) perfect Ly α coupling at early times such that $T_s = T_{\text{IGM}}$

in our observed redshift range, and (2) no X-ray or other heating, thus the IGM continues to cool adiabatically throughout reionization. As with the hot IGM scenario, in these models the reionization histories follow Equation (12) where the only parameters are the redshift and duration, for which we sample the ranges $14 \geq z \geq 6$ and $0.1 \leq \Delta z \leq 4$, respectively. The resulting CMB optical depth for these models covers the range $0.128 \geq \tau_e \geq 0.038$, which is significantly broader than the range currently preferred by Planck, of $0.07 \geq \tau_e \geq 0.046$ at 68% confidence (Planck Collaboration et al. 2016). The models have absorption peaks in the range $\approx 200 - 370$ mK. As before, the only 21 cm fit parameter is the model amplitude.

Figure 8 presents the rejection results for the cold IGM reionization models. We reject a wide range of models, with durations of up to $\Delta z \approx 3$ at 1σ significance, and significances of up to $\approx 60\sigma$ for durations $\Delta z < 0.5$. The average rejection limit across the probed range is $\Delta z \approx 2.2$. In the parameter estimation, the highest sensitivity to these models is achieved using a single 100 MHz window (i.e., the full spectrum) and five polynomial terms. The envelope of the rejection region shows the characteristic shape expected for a fit model consisting of a tanh reionization transition and

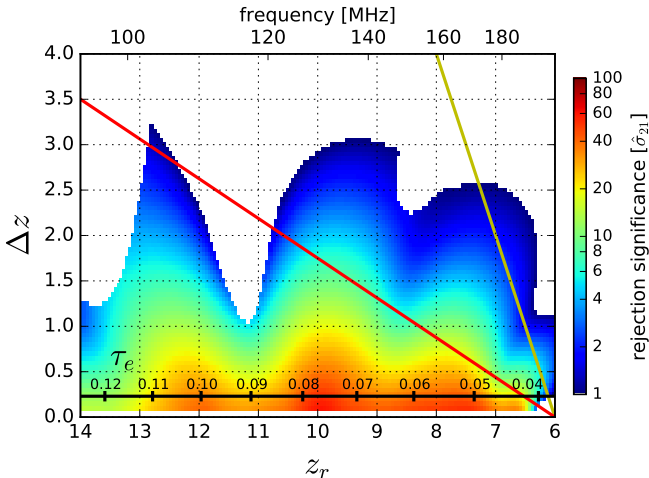


Figure 8. Constraints on cold IGM reionization models from EDGES High-Band. These models assume perfect $\text{Ly}\alpha$ coupling at high redshifts and no IGM heating before or during reionization. The evolution of the neutral fraction, x_{HI} , follows the same tanh-based forms as in the hot IGM scenario. The rejections reach $\approx 60\sigma$ significance for durations $\Delta z < 0.5$. We show a horizontal reference scale for τ_e and two diagonal lines that represent upper limits on Δz inferred from galaxy observations. The yellow line shows the constraint of $\Delta z < 2(z_r - 6)$ as described Section 4.1. The red line shows the more ‘aggressive’ constraint of $x_{\text{HI}} < 1\%$ at $z = 6$. We rule out all of the probed cold IGM reionization models that satisfy $x_{\text{HI}} < 1\%$ at $z = 6$ and a CMB optical depth $0.086 \geq \tau_e \geq 0.038$, which approximately corresponds to the 2σ limits from *Planck*.

a foreground polynomial with a fixed number of terms (see e.g., Pritchard & Loeb 2010; Morandi & Barkana 2012). The redshifts that most significantly depart from this pattern are $11.8 \gtrsim z_r \gtrsim 10.7$ and $z_r \gtrsim 12.8$, which show constraints below the ripple envelope due to higher structure in the spectrum and higher noise, respectively, at the corresponding frequencies. In particular, the dip at $z_r \approx 11$ reduces the rejection limit to $\Delta z \approx 1$ due to the relatively sharp feature in the spectrum at 110–125 MHz.

Inside the figure, we show a horizontal scale with the values of τ_e which, for the range of Δz rejected, are approximately proportional to z_r and weakly dependent on Δz . For reference, we also show two diagonal lines. They represent upper limits on Δz corresponding to (yellow) the constraint $\Delta z < 2(z_r - 6)$ discussed in Section 4.1, and (red) a more ‘aggressive’ constraint that limits the average hydrogen neutral fraction to $x_{\text{HI}} < 1\%$ at $z = 6$, consistent with some of the measurements of high- z quasar spectra introduced in Section 4.1 (e.g., Fan et al. 2006). Reionization scenarios that fall above and to the right of these lines are not allowed by these reference upper limits.

We reject at $\geq 2\sigma$ all models that satisfy $0.086 \geq \tau_e \geq 0.038$ and $x_{\text{HI}} < 1\%$ at $z = 6$. Since this τ_e range approximately matches the $\pm 2\sigma$ range reported by *Planck*, we conclude that a scenario with perfect $\text{Ly}\alpha$ coupling at early times and no IGM heating before or during reionization is strongly inconsistent with current constraints on τ_e and x_{HI} . The strong rejection of these extreme models is, on the other hand, consistent with most theoretical expectations and with the lower limits on the 21 cm spin temperature published by PAPER from interferometric measurements (Jacobs et al. 2015; Ali et al. 2015; Pober et al. 2015; Greig et al. 2016).

4.3. Gaussian Absorption Features

Finally, we probe a broad range of Gaussian models for the global 21 cm absorption trough expected during the First Light era. As discussed above for the cold IGM reionization models, the 21 cm signal is predicted to become visible as an absorption feature against the CMB when $\text{Ly}\alpha$ photons from early stars couple the 21 cm spin temperature to the gas temperature prior to any heating. However, in this more general scenario, the absorption signal ends due to a combination of the eventual X-ray heating of the IGM expected from stellar remnants and, in some cases, reionization. This differs from the cold IGM reionization models that assumed the signal ending solely from reionization. With the current lack of significant constraints, Gaussian shapes continue to be reasonable, generic models for the absorption trough in simulations and analysis of data (Bernardi et al. 2015; Presley et al. 2015; Bernardi et al. 2016). Although some recent physical models depart from Gaussian shapes and exhibit sharper features (e.g., Fialkov & Loeb 2016a; Cohen et al. 2017), several models that predict the trough in our observed band (≥ 90 MHz) resemble a Gaussian to first order (e.g., Sitwell et al. 2014; Kaurov & Gnedin 2016; Mirocha et al. 2017).

Our test models correspond to Gaussians in redshift, and incorporate a skewness term to account for redshift asymmetry:

$$\hat{T}_{21}(z) = -a_{21} \exp \left[-(4 \ln 2) \left(\frac{z - z_r - k_1}{\Delta z - k_2} \right)^2 \right] \times \left\{ 1 + \text{erf} \left[\sqrt{4 \ln 2} \left(\frac{z - z_r - k_1}{\Delta z - k_2} \right) \phi \right] \right\}. \quad (13)$$

The skewness term is based on the error function (erf) and the skewness parameter ϕ . A symmetrical Gaussian is obtained by setting $\phi = 0$. In this model, a_{21} is the peak absorption amplitude, z_r is the peak absorption redshift, and Δz is the FWHM of the trough. The parameters k_1 and k_2 are used to compensate for the change in peak redshift and FWHM as $|\phi|$ increases for fixed z_r and Δz . As with our previous models, the only 21 cm fit parameter is a_{21} . For reference, a redshift symmetrical Gaussian with a FWHM in redshift of $\Delta z = 4$ has a FWHM in frequency of ≈ 25.7 MHz when centered at $z = 14$ (≈ 95 MHz), and of ≈ 94.7 MHz when centered at $z = 7$ (≈ 178 MHz).

Figure 9 (a) shows the 2σ rejection limits for symmetrical Gaussians with reference amplitudes $T_{\text{ref}} = 200, 100, 50,$ and 25 mK. The thick lines represent the results derived from the data, while the thin diagonal lines of the same color correspond to models that produce a brightness temperature of -5 mK at $z = 6$. These diagonal lines illustrate our estimate of generic upper limits for models consistent with a 21 cm signal almost extinguished by $z = 6$. From the EDGES observations, the following reference models can be rejected at $\geq 2\sigma$: (1) for 200 mK amplitude, models with duration $\Delta z \leq 5$ are rejected over the whole band, $14.8 \geq z_r \geq 6.5$; (2) for 100 mK amplitude, models with duration $\Delta z \leq 4$ are rejected over $14.2 \geq z_r \geq 6.5$; (3) for 50 mK amplitude, models with duration $\Delta z \leq 3$ are rejected over $11.8 \geq z_r \geq 6.5$; (4) for 25 mK amplitude, models with duration $\Delta z \leq 2$ are rejected over $11.5 \geq z_r \geq 6.8$. Although not shown for simplicity, large fractions of models below these limits are rejected at $\geq 9\sigma$ significance, especially for 100 and 200 mK amplitudes.

Independently, the reference diagonal upper limits rule out important regions of the $(z_r, \Delta z)$ parameter space. With our data, we reject significant fractions below these limits. In par-

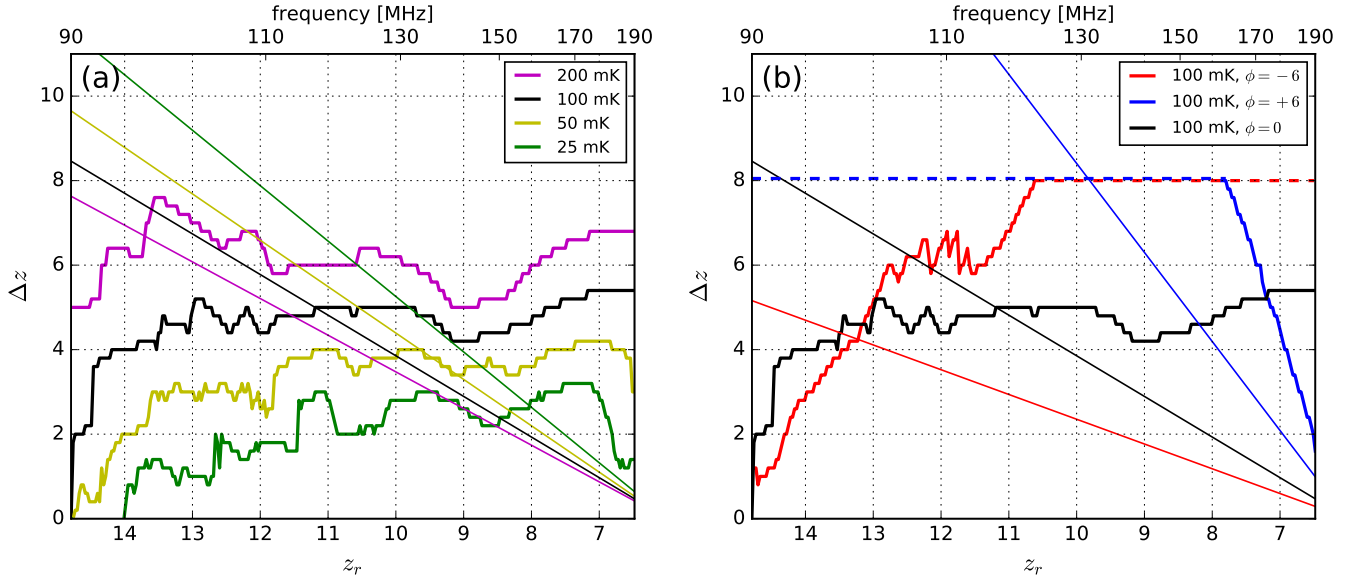


Figure 9. Rejection limits at 2σ significance for Gaussian models of the 21 cm absorption trough expected in the First Light era. The thick lines are the limits derived from the EDGES data and the thin diagonal lines of the same color are reference upper limits for models consistent with a 21 cm signal almost extinguished (brightness temperature between -5 mK and 0 mK) at $z = 6$. These reference upper limits are only shown to reflect that wide Gaussian-like models at low redshifts are inconsistent with scenarios where reionization is completed at $z \approx 6$. (a) Limits for symmetrical Gaussians of amplitudes between 200 and 25 mK. We reject 200 mK Gaussians with duration (FWHM) $\Delta z \leq 5$ over $14.8 \geq z_r \geq 6.5$ and 25 mK Gaussians with $\Delta z \leq 2$ over $11.5 \geq z_r \geq 6.8$. (b) Limits for skewed 100 mK Gaussians with $\phi = -6$ and $\phi = +6$, in addition to the symmetrical Gaussian reference. For both skewness values, the rejection limits grow above $\Delta z = 8$, but we conservatively report a maximum limit of $\Delta z = 8$, depicted as dashed horizontal lines, because that is the total redshift width of our spectrum. We reject large fractions of the permitted regions below the diagonal limits, especially for amplitudes ≥ 100 mK.

ticular, except for a small area above $z_r \approx 13.7$, we rule out all 200 mK Gaussian models in the allowed region.

Figure 9 (b) shows 2σ rejection limits for skewed 100 mK Gaussians with $\phi = -6$ and $\phi = +6$ (see Figure 5 (c)), and also includes, for reference, the symmetrical 100 mK Gaussian limits. We show results for high skewness as clear examples of the effect of model redshift asymmetry on our rejection sensitivity. In particular, models with $\phi = +6$ resemble scenarios of rapid increase in the spin temperature due to strong heating, and/or a rapid decrease in the average hydrogen neutral fraction.

We reject asymmetric Gaussian models with $\phi = -6$ and $+6$ over larger widths than for the symmetrical Gaussian over most of the spectrum, since the asymmetric models have sharper features than the symmetric models for a given width and amplitude. The asymmetric limits are lower than the symmetrical case only at the ends of the observed band. For $\phi = -6$, rejections are low at high z_r because only the smooth half of the model remains inside the spectrum. As the sharp half enters the spectrum and is swept to lower redshifts, our rejection sensitivity increases. The same occurs in the opposite direction for $\phi = +6$. The rejection limit increases above $\Delta z = 8$ for both skewness values in opposite redshift directions. Because our spectrum has a total width of $\Delta z = 14.8 - 6.5 = 8.3$, we conservatively report only a rejection limit capped at $\Delta z = 8$ in these cases. In Figure 9 (b), we also show the diagonal upper limits for models that produce a brightness temperature of -5 mK at $z = 6$. We see that only a small fraction of models with $\phi = -6$ are permitted by the limit, i.e., ones with durations $\Delta z \lesssim 5$ at $z_r = 14.8$, and our data rule out the majority of them. We rule out all the $\phi = +6$ models with $\Delta z \leq 8$ in the region allowed under the limit.

4.4. Calibration Uncertainties

In the constraints presented above, we have assumed that calibration errors do not substantially affect the results. Here, we test that assumption. In order to estimate more broadly the effect of calibration errors on the results, we propagate uncertainties in the calibration parameters through our analysis pipeline following Monsalve et al. (2017). We perform the analysis described above in Section 3 and compute the 21 cm rejection limits after calibrating the data using perturbed calibration parameter values. The perturbations are drawn randomly from Gaussian uncertainty distributions assigned to all relevant calibration parameters. The distributions are based on estimates of possible error levels and centered at the nominal calibration values. Table 1 lists the calibration parameters and their 1σ widths. Running each calibration realization through our pipeline is computationally expensive. Therefore, we only conduct this process for the two 21 cm models with the smallest amplitudes: the 28 mK hot IGM reionization model and the 25 mK symmetrical Gaussian absorption trough model. In both cases, we run 100 realizations with all source uncertainties applied simultaneously. From these realizations, we derive first-order uncertainty estimates for our rejection limits.

We quantify the impact of the calibration uncertainties through the scatter of the 2σ limit on Δz . For the hot IGM models, the average standard deviation of this limit across frequency is 0.1, with a peak of 0.13 at the redshift of peak rejection, $z_r \approx 8.5$. For the 25 mK Gaussian absorption trough model, the average standard deviation is 0.27. The $\sim 10\%$ variation in rejection limits observed in both cases reflects our low sensitivity to a combination of realistic calibration errors. We provide these estimates here as a complement to our nominal results. For future work, we will continue exploring techniques to understand the residual spectral structure in the integrated observation.

Improvements in the instrument and calibration would re-

Table 1
Uncertainties Assigned to Calibration Parameters

Parameter	1σ Uncertainty
Receiver	
Temperature correction	0.1°C
Absolute calibration	from Monsalve et al. (2017)
Antenna Reflection Coefficient	
Magnitude	10^{-4} in voltage ratio (frequency rms)*
Phase	0.1° (frequency rms)*
Antenna and Ground Losses	
Balun length	1 mm
Connector length	0.1 mm
Balun and connector radii	3%
Balun and connector conductivity	1%
Connector teflon permittivity	1%
Panel loss	10%
Ground loss	10% of nominal + 30% from FEKO and CST [†]
Chromaticity Factor	
Sky model	50% of difference between nominal model and sky model from Zheng et al. (2017)
Antenna panel height	2 mm
Antenna panel length	2 mm
Antenna panel width	2 mm
Antenna panel separation	1 mm
Ground plane length	5 cm
Ground plane width	5 cm
Antenna orientation angle	0.5°
Soil conductivity	50%
Soil relative permittivity	50%

Note. — Unless otherwise noted, percentages are given as relative to the nominal value.

* Perturbations modeled as polynomials in frequency, using a number of terms chosen randomly between 1 and 16 (same as for the nominal model), with frequency rms as listed in the Table.

[†] Frequency-independent perturbations to the nominal value plus frequency-dependent perturbations proportional to the FEKO and CST results.

sult in a measurement that represents the sky spectrum with higher fidelity and with lower structure from systematics. This, in turn, could enable to reject more 21 cm models, as well as establish stronger rejections for many of the currently rejected models due to the lower number of terms potentially required in the foreground model for a given frequency range.

5. CONCLUSION

In this paper we evaluate the consistency between three sets of phenomenological models for the global 21 cm signal and the average sky brightness temperature spectrum measured with EDGES High-Band between September 7 and October 26, 2015. In summary, we derive the following constraints for each set of models:

1. We rule out various tanh-based models for reionization that assume the standard hot IGM scenario ($T_s \gg T_{\text{cmb}}$) over the range $14.4 \geq z_r \geq 6.6$. Our peak rejection at 2σ significance is $\Delta z = 1.0$ at $z_r \approx 8.5$. We also reject models with duration $\Delta z \leq 0.8$ over $9 \geq z_r \geq 8$, and $\Delta z \leq 0.4$ over $11.7 \geq z_r \geq 6.7$. These new EDGES results represent a significant improvement with respect to Bowman & Rogers (2010a), and directly complement the upper limits on the reionization duration from secondary CMB anisotropy measurements by SPT. In addition, our peak rejection redshift occurs in the range of current *Planck* estimates for the middle point of reionization.

2. For tanh-based models of reionization that assume an extreme cold IGM scenario with perfect $\text{Ly}\alpha$ coupling at early times (T_s equal to the kinetic gas temperature) and no heating of the IGM before or during reionization, we reject at high significance (up to $\approx 60\sigma$) all models that produce a CMB optical depth in the range $0.086 \geq \tau_e \geq 0.038$ and an average hydrogen neutral fraction $x_{\text{HI}} < 1\%$ at $z = 6$. The rejection of these models is consistent with the expectation of IGM heating during reionization.

3. We rule out a variety of generic Gaussian models for a 21 cm absorption trough in our observed band. As a reference, over the observed spectrum we reject, at $\geq 2\sigma$ significance, redshift symmetrical Gaussians of amplitude 200, 100, 50, and 25 mK with durations $\Delta z \leq 5, 4, 3,$ and $2,$ respectively. For models with skewness, the rejection limit increases over most of the spectrum. In particular, when using $\phi = \pm 6$ in our 100 mK model, the rejection limit increases to $\Delta z = 8$, which is approximately the full width of our measured spectrum.

We propagate our calibration uncertainties to estimate their simultaneous effect on our rejection results and find $\sim 10\%$ scatter in the 2σ rejection limits for the most sensitive models.

Future work is planned to build on this analysis, moving beyond phenomenological models to directly probe astrophysical models for the global 21 cm signal using the EDGES High-Band data. Observations with the EDGES Low-Band system are presently being analyzed and are expected to extend the constraints reported here. Ongoing instrument development is expected to continue to improve the performance of EDGES toward a goal of directly testing the current best estimates for the timing and evolution of reionization.

We are grateful to the reviewer for useful suggestions to improve this paper. We also thank Jordan Mirocha for producing the cold IGM reionization models and for valuable feedback. We finally thank Rennan Barkana, Jack Burns, Steve Furlanetto, Adrian Liu, David Rapetti, Peter Sims, and Keith Tauscher for insightful discussions. This work was supported by the NSF through research awards for the Experiment to Detect the Global EoR Signature (AST-0905990, AST-1207761, and AST-1609450). Raul Monsalve acknowledges support from the NASA Ames Research Center (NNX16AF59G). EDGES is located at the Murchison Radio-astronomy Observatory. We acknowledge the Wajarri Yamatji people as the traditional owners of the Observatory site. We thank CSIRO for providing site infrastructure and support.

REFERENCES

- Ali, Z. S., Parsons, A. R., Zheng, H., et al. 2015, *ApJ*, 809, 61 [4.2]
 Barkana, R., & Loeb, A. 2001, *Phys. Rep.* 349, 125-238 [1]
 Becker, R. H., Fan, X., White, R. L., et al 2001, *AJ*, 122, 6 [4.1]
 Bernardi, G., McQuinn, M., & Greenhill, L. J. 2015, *ApJ*, 799, 90 [2.1.4, 3.1, 4.3]
 Bernardi, G., Zwart, J. T. L., Price, D., et al. 2016, *MNRAS*, 461, 3 [1, 3.1, 4.3]
 Bouwens, R. J., Illingworth, G. D., Oesch, P. A., et al. 2015, *ApJ*, 811, 140 [4.1, 7]
 Bowman, J. D., & Rogers, A. E. E. 2010, *Nature*, 468, 796 [1, 3.2, 4.1, 4.1, 1]
 Bowman, J. D., & Rogers, A. E. E. 2010, Proceedings of the RFI Mitigation Workshop, Groningen, the Netherlands, published online at <http://pos.sissa.it/cgi-bin/reader/conf.cgi?confid=107>, id.30 [1]
 Burns, J. O., Bradley, R., Tauscher, K., et al. 2017, *ApJ*, 844, 33 [1]
 Ciardi, B. & Madau, P. 2003, *ApJ*, 596, 1 [1]

- Cohen, A., Fialkov, A., Barkana, R., & Lotem, M. 2017, [arXiv:1609.02312v2](#) [1, 4.3]
- Chornock, R., Berger, E., Fox, D. B., et al. 2013, *ApJ*, 774, 26 [4.1]
- Choudhury T. R., Puchwein E., Haehnelt M. G., & Bolton J. S. 2015 *MNRAS*, 452, 1 [4.1]
- Das, S., Louis, T., Nolita, M. R., et al. 2014, *J. Cosmology Astropart. Phys.*, 4, 14 [4.1]
- Fan, X., Strauss, M. A., Becker, R. H., et al. 2006, *AJ*, 132, 117 [4.1, 4.2]
- Fialkov, A., & Loeb, A. 2016, *ApJ*, 821, 59 [1, 4.3]
- Fialkov, A., Cohen, A., Barkana, R., & Silk, J. 2016, *MNRAS*, 462, 4 [1, 1]
- Field, G. B. 1958, *Proc. IRE* 46, 240 [1]
- Furlanetto, S. R. 2006, *MNRAS*, 371, 2 [1, 4.1]
- Furlanetto, S. R., Oh, S. P., & Briggs, F. H. 2006, *Phys. Rep.*, 433, 181 [1, 4.1, 4.1]
- Gallerani, S., Choudhury, T. R., & Ferrara, A. 2006, *MNRAS*, 370, 3 [4.1]
- George, E. M., Reichardt, C. L., Aird, K. A., et al. 2015, *ApJ*, 799, 177 [4.1, 7]
- Gnedin, N. Y., & Shaver, P. A. 2004, *ApJ*, 608, 2 [1, 1]
- Greig, B., Mesinger, A., & Pober, J. C. 2016, *MNRAS*, 455, 4 [4.2]
- Greig, B., & Mesinger, A. 2017, *MNRAS*, 465, 4 [1, 7, 4.1]
- Greig, B., Mesinger, A., Haiman, Z., Simcoe, R. A. 2017, *MNRAS*, 466, 4 [4.1]
- Guzmán A. E., May J., Alvarez H., Maeda K. 2011, *A&AS*, 525, A138 [2.1.4]
- Harker, G. J. A., Mirocha, J., Burns, J. O., Pritchard, J. R. 2016, *MNRAS*, 455, 4 [4.1]
- Haslam, C. G. T., Salter, C. J., Stoffel, H., & Wilson, W. E. 1982, *A&AS*, 47, 1 [2.1.4]
- Hinshaw, G., Larson, D., Komatsu, E., et al. 2013, *ApJS*, 208, 19 [4.1]
- Jacobs, D. C., Pober, J. C., Parsons, A. R., et al 2015, *ApJ*, 801, 51 [4.2]
- Kaurov, A. A., & Gnedin, N. Y. 2016, *ApJ*, 824, 114 [1, 4.3]
- Kogut, A. 2012, *ApJ*, 753, 2 [3.1]
- Lewis, A. 2008, *Phys. Rev. D*, 78, 023002 [4.1]
- Liu, A., Pritchard, J. R., Tegmark, M., & Loeb, A. 2013, *Phys. Rev. D*, 87, 043002 [4.1]
- Madau, P., Meiksin, A., & Rees, M. J. 1997, *ApJ*, 475, 429 [1, 4.1]
- Madau P., & Haardt, F. 2015, *ApJL*, 813, L8 [1]
- McGreer, I. D., Mesinger, A., D'Odorico, V. 2015, *MNRAS*, 447, 1 [4.1]
- Mesinger, A. 2010, *MNRAS*, 407, 2 [4.1]
- Mesinger, A., Ferrara, A., & Spiegel, D. S. 2013, *MNRAS*, 431, 621-637 [1, 1, 4.1]
- Mirocha, J., Harker, G. J. A., & Burns, J. O. 2013, *ApJ*, 777, 118 [1]
- Mirocha, J., Harker, G. J. A., & Burns, J. O. 2015, *ApJ*, 813, 11 [1, 4.1]
- Mirocha, J., Furlanetto, S. R., & Sun, G. 2017, *MNRAS*, 464, 1365-1379 [1, 4.3]
- Mitra, S., Choudhury, T., R., Ferrara, A. 2015, *MNRAS*, 454, L76-L80 [7, 4.1]
- Monsalve, R. A., Rogers, A. E. E., Mozdzen, T. J., & Bowman, J. D. 2016, *IEEE Trans. Microw. Theory Tech.*, 64, 8 [1, 2.1.1, 2.1.2]
- Monsalve, R. A., Rogers, A. E. E., Bowman, J. D., & Mozdzen, T. J. 2017, *ApJ*, 835, 49 [1, 2, 2.1.1, 2.1.2, 3.1, 4.4, 1]
- Morandi, A., & Barkana, R. 2012, *MNRAS*, 424, 2551 [4.1, 4.2]
- Mozdzen, T. J., Bowman, J. D., Monsalve, R. A., Rogers, A. E. E. 2016, *MNRAS*, 455, 4 [1, 2, 2.1.4]
- Mozdzen, T. J., Bowman, J. D., Monsalve, R. A., Rogers, A. E. E. 2016, *MNRAS*, 464, 4995-5002 [1, 2, 2.1.4, 3.1]
- Offringa, A. R., Wayth, R. B., Hurley-Walker, N., et al. 2015, *PASA*, 32, e008 [1]
- Ouchi, M., Shimasaku, K., Furusawa, H., et al 2010, *ApJ*, 723, 1 [4.1]
- Planck Collaboration XLVII 2016, *A&A*, 596, A108 [4.1, 7, 4.2]
- Pober, J. C., Ali, Z. S., Parsons, A. R., et al. 2015, *ApJ*, 809, 62 [4.2]
- Presley, M. E., Liu, A., & Parsons, A. R. 2015, *ApJ*, 809, 18 [4.3]
- Pritchard, J. R., & Furlanetto, S. R. 2007, *MNRAS*, 376, 1680-1694 [1]
- Pritchard, J. R., & Loeb, A. 2010, *Phys. Rev. D*, 82, 023006 [4.1, 4.2]
- Pritchard, J. R., & Loeb, A. 2012, *Rep. Prog. Phys.* 75, 086901 [1, 4.1]
- Roberts, W. K. 1957, *Proc IRE*, 1624 [2]
- Robertson, B. E., Ellis, R. S., Furlanetto, S. R., & Dunlop, J. S. 2015, *ApJL*, 802, L19 [7, 4.1]
- Rogers, A. E. E., & Bowman, J. D. 2008, *AJ*, 136, 641 [1]
- Rogers, A. E. E., & Bowman, J. D. 2012, *Radio Sci.*, 47, RS0K06 [1, 2, 2.1.1]
- Rogers, A. E. E., Bowman, J. D., Vierinen, J., Monsalve, R., & Mozdzen, T. 2015, *Radio Sci.*, 50, 130 [1]
- Sathyanarayana Rao, M., Subrahmanyam, R., Udaya Shankar, N., & Chlubna, J. 2017, *ApJ*, 840, 33 [3.1]
- Schroeder, J., Mesinger, A., & Haiman, Z. 2013, *MNRAS*, 428, 4 [4.1]
- Shaver, P. A., Windhorst, R. A., Madau, P., & de Bruyn, A. G. 1999, *A&A*, 345, 380 [1, 1]
- Singh, S., Subrahmanyam, R., Udaya Shankar, N., Sathyanarayana Rao, M., Fialkov, A., Cohen, A., Barkana, R., Girish, B. S., Raghunathan, A., Somashekar, R., and Srivani, K. S. 2017, [arXiv:1703.06647](#) [1]
- Sitwell, M., Mesinger, A., Ma, Y.Z., Sigurdson, K., 2014, *MNRAS*, 438, 3 [1, 4.3]
- Sutinjo, A. T., Colegate, T. M., Wayth, R. B. et al. 2015, *IEEE Trans. Antennas Propag.*, 63, 12 [2.1.3]
- Tanaka, T. L., O'Leary, R. M., & Perna, R. 2016, *MNRAS*, 455, 3 [1]
- Tilvi, V., Papovich, C., Finkelstein, S. L., Long, J., et al. 2014, *ApJ*, 794, 5 [4.1]
- Vedantham, H. K., Koopmans, L. V. E., de Bruyn, A. G., et al. 2014, *MNRAS*, 437, 1056-1069 [2.1.4]
- Voytek, T. C., Natarajan, A., Garcia, J. M. J., Peterson, J. B., & López-Cruz, O. 2014, *ApJL*, 782, L9 [1, 3.1]
- Wouthuysen, S. A. 1952, *AJ*, 57, 31 [1]
- Zaldarriaga, M., Furlanetto, S. R., & Hernquist, L. 2004, *ApJ*, 608, 622 [1]
- Zheng, H., Tegmark, M., Dillon, J. S., Kim, D. A., Liu, A., Neben, A. R., Jonas, J., Reich P., and Reich, W. 2017, *MNRAS*, 464, 3486-3497 [1]